MICROSTRUCTURE AND MECHANICAL PROPERTIES OF TIN-BISMUTH SOLDER ALLOY REINFORCED BY ANTIMONY OXIDE NANOPARTICLES

Shereen M. Abdelaziz[1,3], H. Y. Zahran[2,3], A. F. Abd El-Rehim[2,3]
[1] Physics Department, Faculty of Science, Qassim University,
P.O. Box 6666, Buraydah 51452, Saudi Arabia.
[2] Physics Department, Faculty of Science, King Khalid University,
P.O. Box 9004, Abha 61413, Saudi Arabia.
[3] Physics Department, Faculty of Education, Ain Shams University,
P.O. Box 5101, Heliopolis 11771, Roxy, Cairo, Egypt

ABSTRACT

The influence of 1wt% Sb_2O_3 nanoparticles addition on the microstructure and mechanical properties of Sn-3wt% Bi solder alloy has been investigated. X-ray diffraction (XRD) and scanning electron microscope (SEM) were utilized *to* observe *the* microstructure of *Sn-Bi solder (alloy A) and Sn-Bi-Sb_2O_3 composite solder (alloy B). The mechanical properties of both alloys* were *characterized by using Vickers microhardness tests over the range of aging temperature 300-363 K. Experimental results indicated the hardness values of alloy B are higher than in alloy A. Furthermore, the hardness of both alloys decreased as the aging temperature increased exhibiting maxima at 333K. Values of stress exponent were found to be in the range of 7 to 18 for both alloys. The average values of the activation energy of both alloys A and B was found to be 68 and 74 kJ/mol respectively.*

KEYWORDS: *Sn-Bi Based Solders; Sb_2O_3 Nanoparticles; Microstructure; Hardness*

I. INTRODUCTION

A global movement away from using lead in the manufacture of industrial parts had led researchers to develop new lead-free solders [1–3]. Sn–Bi solders can be considered as an alternative candidate for lead-free solder materials. The advantages of Sn–Bi solders include low melting point which enables lower soldering temperature, superior creep resistance, low thermal expansion coefficient, good wettability, and low cost [4].

Several authors have examined the microstructure evolution and mechanical characteristics of non eutectic Sn–Bi solder alloy. The effect of testing temperature and grain size on the creep characteristics of Sn–3wt% Bi alloy has been investigated [5]. It was found that increasing grain size in the temperature range 303–333 K leads to a significant improvement in the creep resistance. The mean activation energy values for both transient and steady state creep stages ranged from 67 to 72 kJ/mol. These values indicated that the dominant creep mechanism is the grain-boundary sliding. Mitlin et al. [6] studied the influence of Bi content on the steady state creep characteristics of Sn–Bi alloys. They concluded that increasing Bi concentration enhances the creep strength of Sn–Bi alloys. Mahmudi et al. [7] performed indentation creep experiments at room temperature on Sn–Bi alloys with different Bi concentrations. Results showed that the creep rate decreased with increasing Bi concentration, leading to an improvement in the creep resistance in more concentrated alloys. More recently, Lai and Ye [8] investigated the microstructure evolution and mechanical characteristics of Sn–xBi (x = 10, 20, 25, and 35) solder alloys. The microstructure of Sn–10Bi and Sn–20Bi solder was constituted by Bi particle and β-Sn phase while the microstructure of Sn–25Bi and Sn–35Bi solder

was consisted of eutectic phase and β-Sn phase. The Sn–20Bi solder showed the highest ultimate tensile load (UTL) in notch tensile test among all solders tested.
Indentation creep tests have been performed at room temperature to study the effect of cooling rate on the microstructure and creep characteristics of the cast Sn-Bi solder alloys [9]. The stress exponents were found to be 14.5 and 9.5 for quenched and slowly cooled conditions respectively. The creep characteristics of Sn-5wt% Bi alloy have been investigated over the range of temperature 305-373 K under constant applied stresses [10]. The variation in the creep parameters with temperature indicated one transition point at 340 K. The activation energy values of the steady state creep were found to be 62 and 87 kJ/mol before and after the transition temperature respectively.
One attractive viable approach to enhance the properties of the solder is to create a composite solder by the addition of second reinforcing particles to the solder matrix. Examples of such reinforcements are fine oxide particles, intermetallic, metallic powders, or carbon fibers [11–14]. Lee et al. [15] investigated the effect of nanosized SiC particles addition on the mechanical characteristics and microstructure of eutectic Sn-58wt% Bi alloy. Results showed that adding SiC nanoparticles improved the shear strength of the binary alloy. This was ascribed to fine-grained microstructure and strengthening effect by nanosized SiC particles. Effects of different weight percent of nanosized graphite particles on spreadability, microstructure, and mechanical properties of Sn-Bi solder were systematically studied [16]. It was demonstrated that the microstructure of Sn-Bi-graphite composite solder is refined gradually with increasing the concentration of nanosized graphite particles. Moreover, Sn-Bi-0.07wt% graphite composite solder has a better creep resistance than Sn-Bi solder. According to the reviewed literature, no attempts have been reported to reinforce the lead-free Sn-Bi solder alloy using Sb_2O_3 nanoparticles as reinforcement. Consequently, the present study is devoted to study the effect of nanosized Sb_2O_3 particles addition on the microstructure and mechanical characteristics of the Sn-3wt% Bi solder alloy.

II. EXPERIMENTAL PROCEDURES

2.1 Materials

Sn-3wt% Bi solder alloy (alloy A) and Sn-3wt% Bi-1wt% Sb_2O_3 composite solder alloy (alloy B) were prepared from Sn (99.99%), Bi (99.99%), and nano Sb_2O_3 (50-100 nm: 99.99%) (Sigma-Aldrich) by vacuum melting. The starting raw materials were melted and mixed in high purity graphite crucibles under Ar atmosphere at a temperature of 623 K. The molten alloys were cast into a steel mold to prepare the chill cast ingots. After solidification, the cast ingots of diameter 10mm were homogenized at 423 K for 24 h and slowly cooled to room temperature. The ingots were cut into 10mm × 10mm × 1mm slices for mechanical measurements and microstructure characterization. The slices of two alloys were aged at different temperatures ranging from 300 to 363 K for 2 h followed by quenching into ice water at 273 K.

2.2 Microstructural characterization

The slices used for microstructural analysis were ground and polished according to standard metallographic techniques. To reveal the grain boundaries of the slices, a solution of 4ml HNO_3 and 96 ml C_2H_5OH was used as an etchant. A JEOL JSM-6360LV SEM operated at 20 kV equipped with an energy dispersive X-ray spectrometry (EDX) system was used to examine the microstructure of the slices. X-ray diffraction (XRD) is widely used for phase identification of unknown crystalline materials. The phases were identified using an X-ray diffractometer (CuKα, Shimadzu LabXRD-6000) operated at 30 mA and 40 kV at diffraction angle 2θ from 20° to 90°.

2.3 Mechanical properties measurements

Hardness measurements were performed on the metallographically polished surface of samples using a Vickers Shimadzu microhardness tester to characterize the mechanical properties of the two alloys A and B. Vickers microhardness values (H_v) were computed from the following expression [17]:

$$H_v = 1.8545\frac{F}{d^2} \quad (1)$$

where F is the applied load in kg and *d* is the average indentation diagonal length in mm. The hardness values (H_v) were measured using a Vickers indenter at 10, 50, and 100 g loads for dwell times 10, 30, 40, and 60 s. Ten readings of different indentations were examined on the flat and polished surface of the samples. The mean value of the different measurements was used as the hardness value of each sample.

III. RESULTS AND DISCUSSION

The variation of hardness values, H_v, with aging temperature, *T*, at different dwell times under constant applied loads of 10, 50, and 100 g for both solder alloys is presented in Fig. 1. It is clear that:

i. the hardness values, H_v, decreased with increasing the applied load and/or the dwell time.
ii. under the same test conditions, the hardness values of alloy A are smaller than in alloy B.
iii. the hardness values decreased gradually with increasing aging temperature exhibiting abrupt increase at about 333 K.

The variation of H_v with aging temperature, as shown in Fig. 1, can be attributed to the formation or dissolution of the Bi-rich phase and the presence of dispersive nanosized Sb_2O_3 particles. In the aging temperature range 300-363 K, the two alloys show temperature regions. The first region is below 333 K and the second region is above this temperature. The binary phase diagram of Sn–Bi system is shown in Fig. 2. It is a simple eutectic system without any intermetallic compound [18]. There is a significant solid solubility of Bi in Sn, up to 21wt% Bi, at the eutectic temperature of 139 °C (412 K). The liquidus temperature decreases with increasing Bi concentration from ~ 232°C (505 K) for pure Sn to 139 °C at the eutectic Sn-57wt% Bi. The corresponding concentration of the Sn–Bi alloy examined in the present study is displayed as the vertical line in the binary phase diagram. During solidification process, the Sn-rich phase would form first from the liquid and then Bi solid solute atoms precipitates at or near the grain boundaries of Sn matrix. In the first range of aging temperature below 333 K, the decline in hardness values with increasing temperature for both alloy A and B at all dwell times and applied loads could be explained as being due to the coarsening process of Bi atoms to form Bi-rich phase. Thus, the interaction between Bi solute atoms and dislocations will be lowered leading to the observed decrease in the hardness values for both alloys. These results agree well with those previously reported by Al-Ganainy et al. [10] who stated that the creep parameters increased with increasing temperature from 305 to 328 K for Sn–5wt% Bi alloy.

The anomalous behavior in the hardness values at 333 K can be ascribed to the dissolution of Bi-rich phase in the β-Sn matrix this transformation temperature (333 K). According to the binary phase diagram (Fig. 2), when the aging temperature increases up to 333 K the Bi-rich phase ejects Bi atoms and converts to Sn-rich phase. Consequently, the Bi atoms will move towards grain boundaries of Sn-matrix and pin mobile dislocations [19]. This limits the grain boundary movement and enhances the hardness of the two alloys. This explanation is strongly supported by both SEM and EDX. The SEM images and the corresponding EDX spectra of both alloys A and B heated at 333 K are presented in Fig. 3a and b respectively. From Fig.3, it is clearly seen that the gray matrix is the Sn-rich phase, and the white precipitates on the grain boundaries are pure Bi particles. This is in good agreement with the structure reported by Mahmudi et al. [7]. According to the EDX spectra, the alloy A was found to contain Sn and Bi, while the alloy B was found to contain Sn, Bi, O, and Sb. In order to observe the uniform distribution of nanosized Sb_2O_3 particles inside the β-Sn matrix, SEM micrograph of alloy B was taken at a high magnification (Fig. 4). As it is clearly seen, the Sb_2O_3 nanoparticles are uniformly distributed in the Sn-Bi-Sb_2O_3 composite solder (alloy B) without aggregation.

During the entire second range of aging temperature (333-363 K), the decrease in the hardness values (Fig. 1) could be due to the dissolving of the Bi solute atoms in the β-Sn matrix (see Fig. 5). The dissolving process lowers the interaction between dislocations and Bi atoms. Accordingly, it is easier for the dislocations to breakaway from the pinning centers that act as barriers leading to the softening behavior [20]. Moreover, the higher aging temperature, the higher is the grain size obtained (Fig. 5). When the grain size increases, the barriers for dislocations movement decrease which eventually leads to the decrease in the hardness values.

Comparing the hardness values of the two alloys A and B under the same test conditions, it could be observed that these values are higher in alloy B than in alloy A (Fig. 1). Comparing the micrographs

presented in Fig. 3 (a and b), it could be seen that the microstructure in both alloys is the same but the number of fine Bi particles is different.

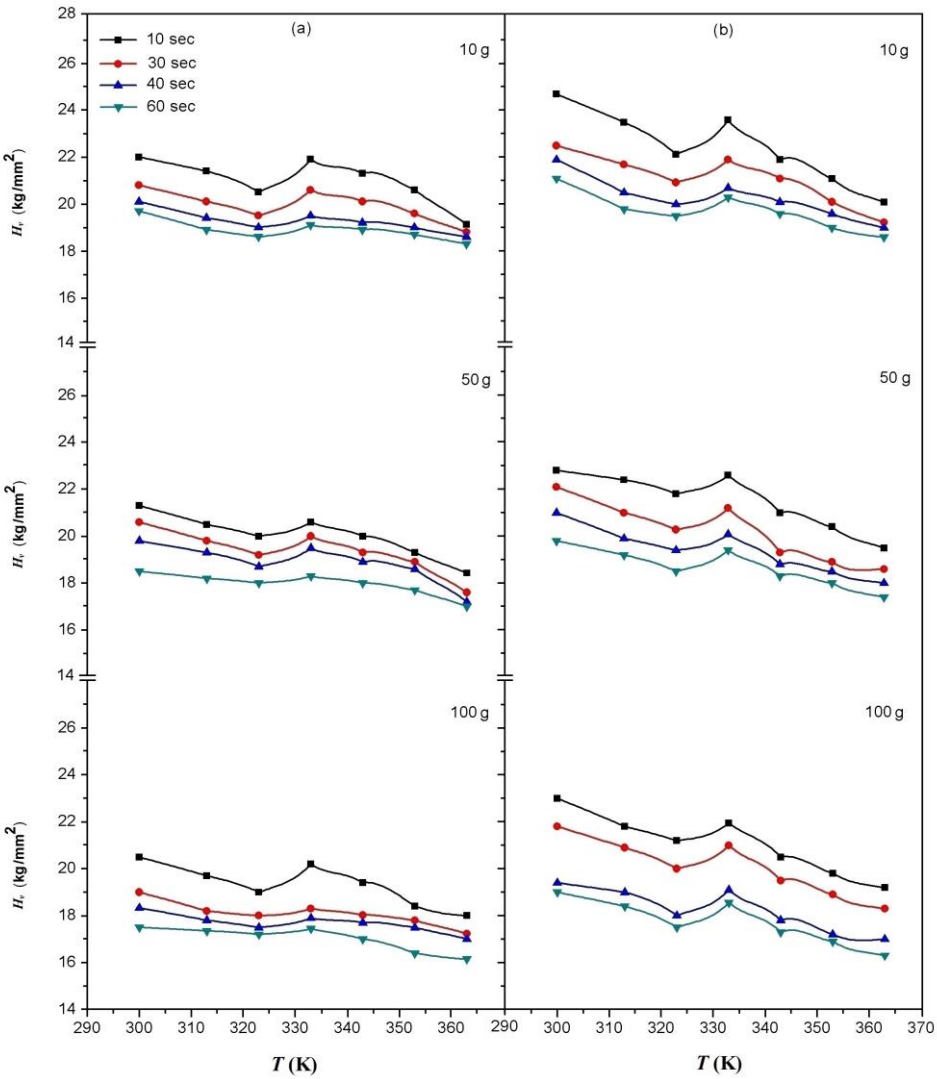

Fig. 1 Hardness versus aging temperature plot for a) alloy A and, b) alloy B at different dwell times and applied loads.

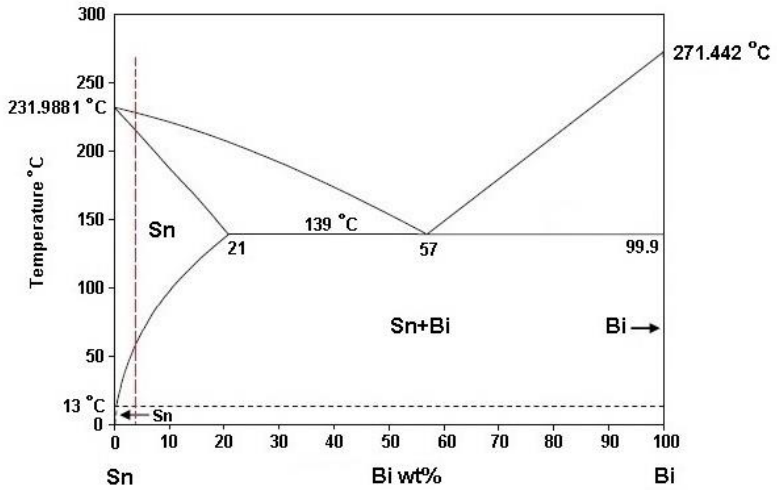

Fig. 2 The binary phase diagram of Sn-Bi alloy showing the concentration evaluated in this study.

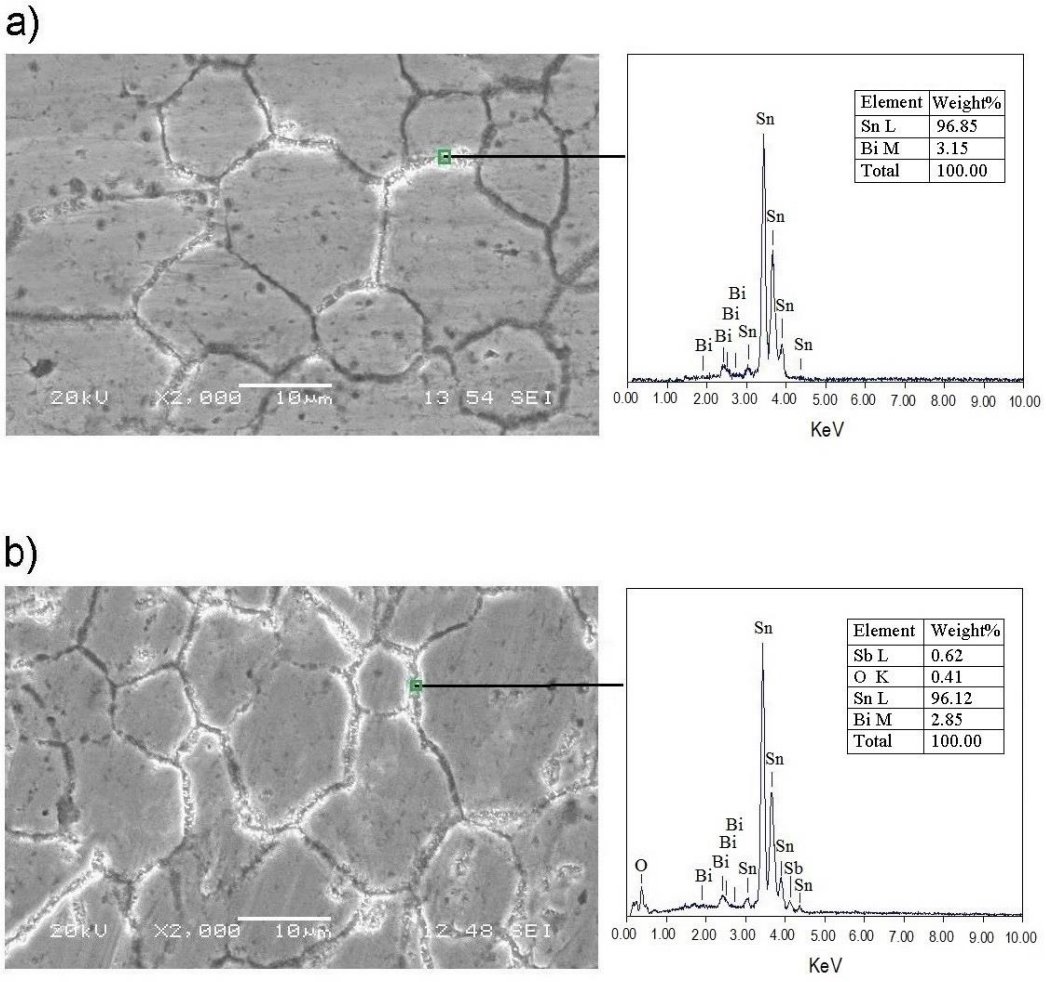

Fig. 3 SEM images (left) and the corresponding EDX spectrum (right) of a) alloy A, and b) alloy B aged at 333 K showing the precipitation of fine Bi particles at the grain boundaries of Sn-rich phase.

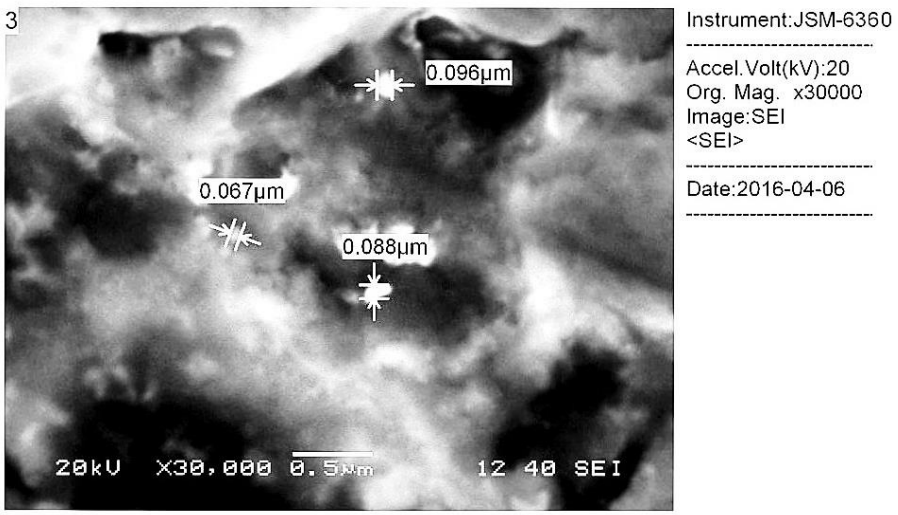

Fig. 4 SEM image showing the distribution of Sb_2O_3 nanoparticles within the Sn-matrix in the alloy B.

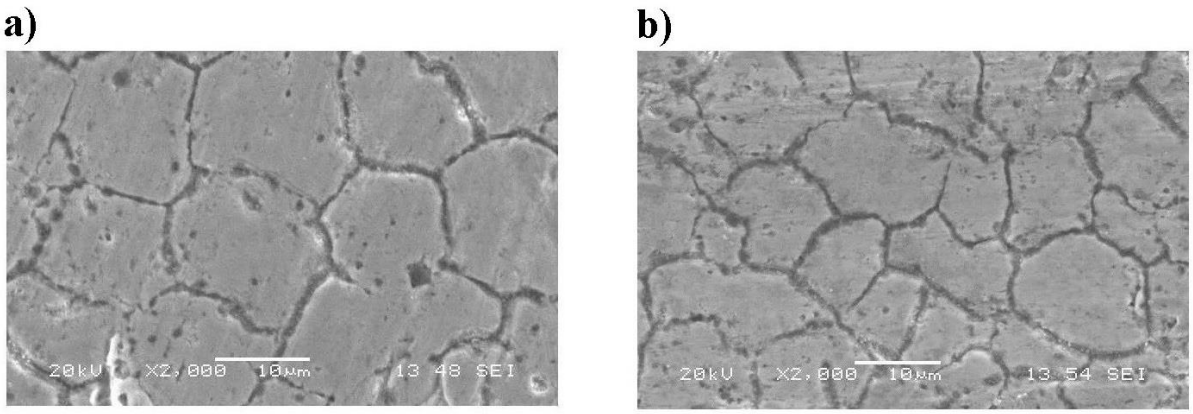

Fig. 5 SEM images of a) alloy A, and b) alloy B aged at 353 K showing the dissolving of fine Bi particles.

It is clear that the Bi particles are less dense in alloy A than in alloy B which may account for the higher values of hardness in alloy B than in alloy A. This could be rendered as being due to the presence of Sb_2O_3 nanoparticles which may act as the nucleation sites for the Bi particles. This is in accord with the previous work of Chang et al. [12] who found that the addition of nanosized TiO_2 particles **t**o Sn-Ag-Cu solder alloy increases its hardness. Moreover, the enhanced hardness values of alloy B are in a fair agreement with the classical theory of dispersion strengthening created by the addition of Sb_2O_3 nanoparticles [21]. These nanosized Sb_2O_3 particles act as potential pinning centers for the dislocations motion and grain boundaries. The increase in hardness values in the case of alloy B with the addition of Sb_2O_3 reinforcements was expected due to the grain refinement of the alloy B compared with those of alloy A. Close examination of a number of SEM micrographs in both alloys (Figs 3 and 5) indicated that relatively finer grains in the case of Sn-Bi-Sb_2O_3 composite solder (alloy B) when compared to that of Sn-Bi solder (alloy A). The fine-grained microstructure possesses a large grain boundary area resulting in high interface energy; consequently, the hardness values increased [22]. Furthermore, nanoparticles can act as pinning sites which inhibited the mobility of dislocations that concentrated around grain boundaries [23]. Similar trends are also found in other solder alloys [13,15,24].

The morphological (SEM and EDX) analysis is well confirmed by the XRD results. Figure 6 exhibits the profiles of XRD patterns of the two alloys A and B at different aging temperatures. The pattern of alloy A (Fig. 6a) indicates two phases, namely; Sn-rich phase (β-Sn matrix) and Bi-rich phase which matched with JCDPS cards No. 4-0673 for Sn and No. 85-1331 for Bi. No peaks related to inter-metallic phase between Sn and Bi are observed. The pattern of alloy B (Fig. 6b) is characterized by the presence of the same two phases plus two additional peaks for Bi-rich phase and Sb_2O_3 nanoparticles. The crystalline phase of antimony oxide (Sb_2O_3) was identified by comparing with JCPDS card No. 71-0383. This means that the Sb_2O_3 nanoparticles were successfully blended with the alloy A. The most interesting feature of XRD patterns presented in Fig. 6 is that the relative intensities of the diffraction peaks distinctive for Bi particles in alloy B (Sb_2O_3 containing) are higher than that in alloy A. For both alloys A and B, the intensities of these peaks significantly decreased with increasing the aging temperature exhibiting maxima at 333 K. Moreover, Bi particles diffraction peaks are completely disappeared at 363K for alloy A (Fig. 6a) while there is a little appearance for them in alloy B (Fig. 6b). XRD data can be used to determine the average crystallite size, η, and lattice strain, ε, for the Sn-rich phase using the following equation [25]:

$$\frac{\beta\cos\theta}{\lambda} = \frac{1}{\eta} + \frac{(2\varepsilon\sin\theta)}{\lambda} \qquad (2)$$

where λ is the wavelength of radiation used, θ is the Bragg angle and β is the full-width at half-maximum (FWHM) measured in radian. The plots of $(\beta\cos\theta)/\lambda$ versus $(\sin\theta)/\lambda$ are straight lines. The half of slope of these straight lines gives the lattice strain, ε. The reciprocal of intercepts on the $(\beta\cos\theta)/\lambda$ axis gives the average crystallite size, η. The dislocation density (δ) is defined as the length of dislocation lines per unit volume of the crystal and calculated by using the formula [26]:

$$\delta = \frac{1}{\eta^2} \quad (3)$$

The aging temperature dependence of the average crystallite size, η, lattice strain, ε, and the dislocation density, δ, for both alloys is depicted in Fig. 7. It can be directly observed that the lattice strain and dislocation density decreased with increasing aging temperature exhibiting maxima at 333 K while the average crystallite size followed the opposite behavior with an increase in aging temperature. This can be attributed to the annihilation of lattice imperfections such as dislocations and the reduction of total grain boundary area per unit volume during heating.

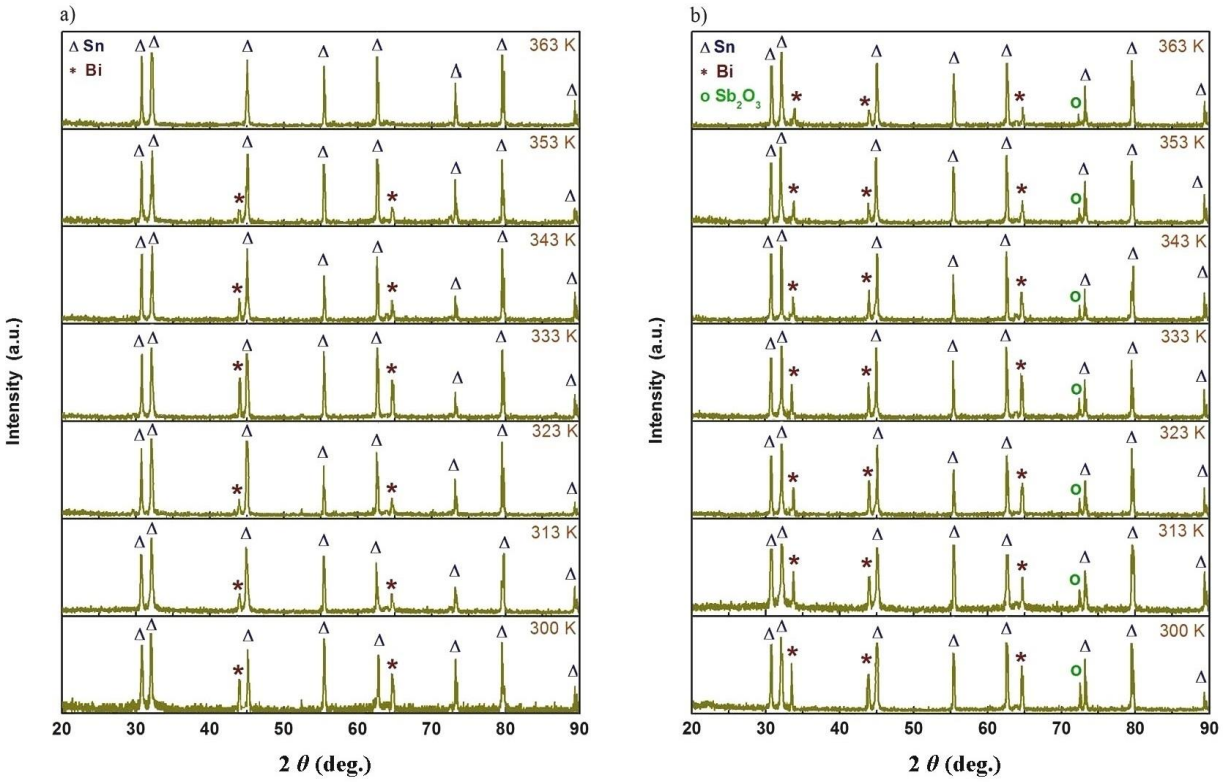

Fig. 6 X-ray diffraction patterns for a) alloy A, and b) alloy B at different aging temperatures.

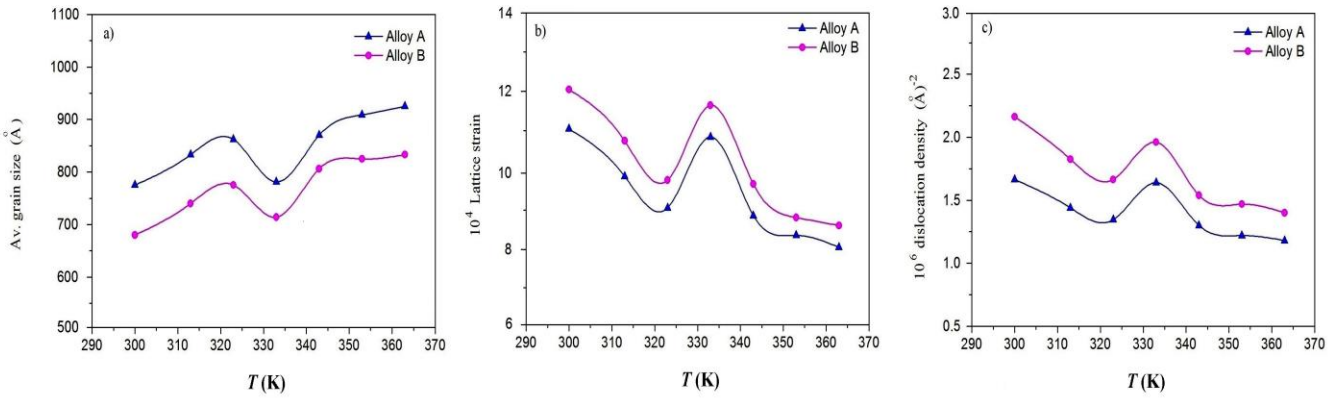

Fig. 7 Aging temperature dependence of a) average crystallite size, b) lattice strain, and c) dislocation density for both alloys A and B.

One can observe that the lattice strain, η, and dislocation density, δ, of Sn-rich phase for alloy B are higher than that in alloy A. This increment can be referred to the presence of Sb_2O_3 nanoparticles which generates additional impurity defects in alloy B. Moreover, the relationship between the dislocation density and the hardness evaluation in metals and alloys was previously investigated [27].

It has been reported [28] that increasing of dislocations density and the mutual interactions between them increase the hardness. This explains the observed increase in hardness values, H_v, and dislocation density, δ, for alloy B with the addition of Sb_2O_3 nanoparticles.

According to Sargent and Ashby model [29], the stress exponent, n, in the steady state indentation creep can be evaluated from the slopes of the straight lines relating ln H_v and ln t (t is dwell time in seconds) at different constant aging temperatures. The slope of these lines is (-1/n) from which the stress exponent, n was determined. The variation in the stress exponent, n, with aging temperature, T, is depicted in Fig. 8. The n values of both alloys ranging from 7 to 18. The stress exponent values can be used to determine the type of deformation mechanism. It was reported [30] that Harper-Dorn dislocation creep or Coble diffusional creep is associated with n values around 1. The viscous glide of dislocations rate controlling mechanism leads to n values close to 3. When the stress exponent is ranging from 5-7, dislocation climb creep is thought to be the rate controlling mechanism. Anomalously high stress exponent values have been noted in composite alloys [31]. Many authors [32-34] postulated that the reinforcement particles in the composite alloys served as effective barriers for dislocations movement and gave rise to the high stress exponent values obtained in this work. These results are in good agreement with the work of Mahmudi et al. [7] who found that the stress exponent of Sn-5wt% Bi solder alloy ranging from 9 to 15 at room temperature.

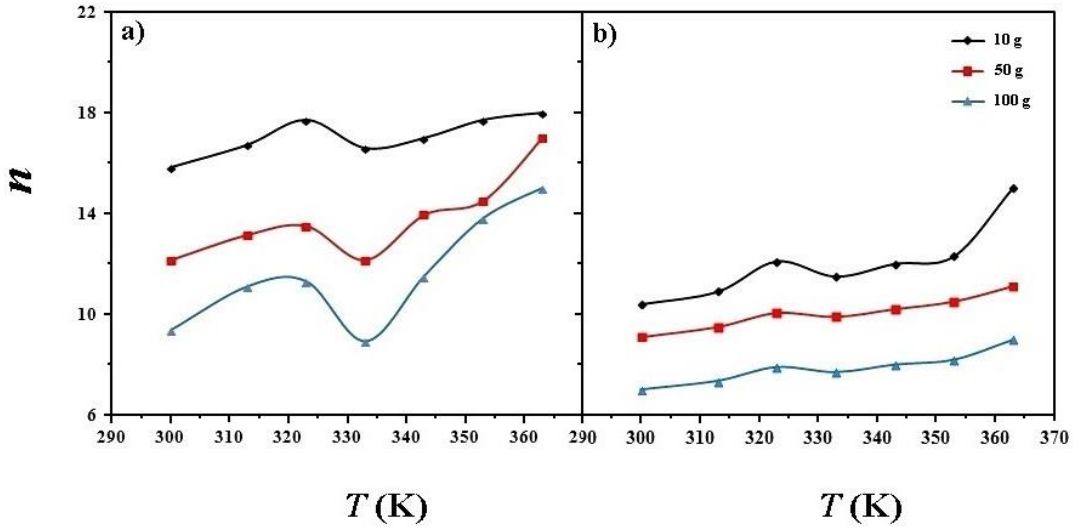

Fig. 8 Aging temperature dependence of the stress exponent, n, for a) alloy A, and b) alloy B at different applied loads.

The energy activating the indentation creep process, Q_c, in the present work has been determined from the relation [31,35]:

$$Q_c = \frac{R\log(t_1/t_2)}{(1/T_1)-(1/T_2)} \quad (4)$$

where R is the universal gas constant, t_1 and t_2 are dwell times to reach a given hardness value at temperatures T_1 and T_2, respectively. The activation energy of both alloys was evaluated from the slopes of the straight lines relating log t versus (1/RT) at constant hardness values (Fig. 9). Table 1 demonstrated the values of activation energy for both alloys. The mean values of the activation energy was found to be ~ 68 and 74 kJ/mol for the two alloys A and B respectively. From Fig. 9 and Table 1, it can be seen that the average value of activation energy for alloy A is smaller than in alloy B. This could be attributed to the refining effect of nanosized Sb_2O_3 particles which is associated with the formation of large number of second-phase particles (obstacles) in the alloy B that needs higher energies than in alloy A. Knowledge of the activation energy enables the identification of the mechanisms controlling the deformation process.

An examination of the existing literature on creep mechanisms of Sn and Sn-based alloys showed significant discrepancies in the activation energy and stress exponent. Mitlin et al. [6] reported that the

activation energy of pure Sn fell in the range between 49 and 107 kJ/mol at low and high temperature creep respectively.

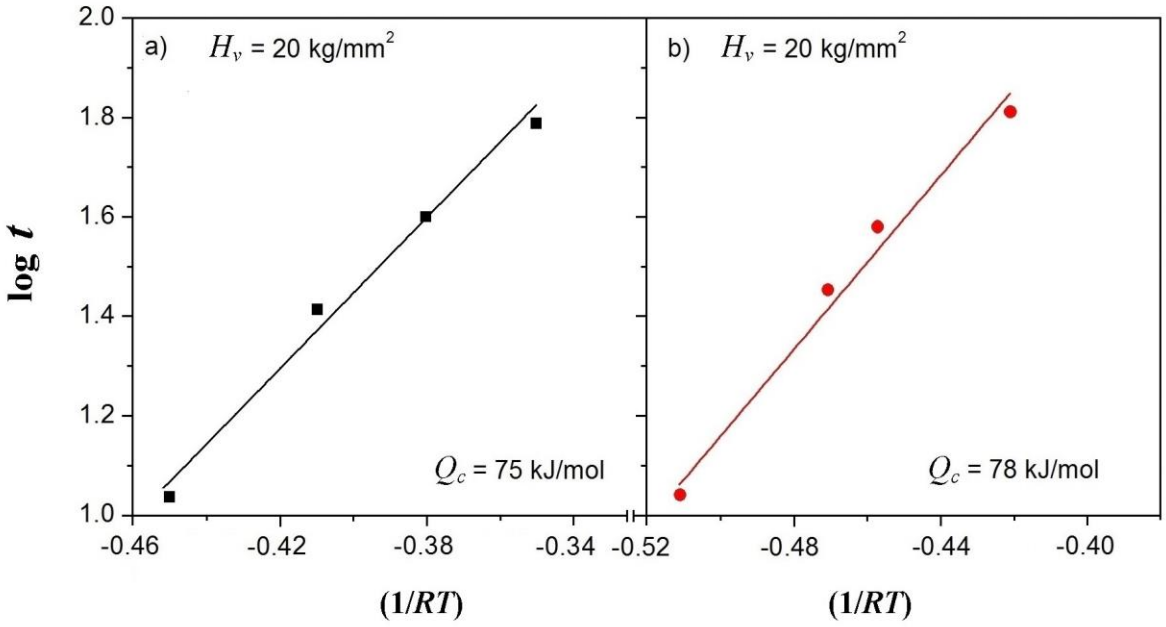

Fig. 9 Representative relationship between log *t* versus (1/*RT*) at applied load of 10 g for a) alloy A, and b) alloy B.

Table 1 Values of activation energy obtained for both alloys A and B at different applied loads.

Loads (gm)	Activation energy (kJ/mol)	
	Alloy A	Alloy B
10	75 at H_v = 20 kg/mm^2	78 at H_v = 20 kg/mm^2
50	65.8 at H_v = 18 kg/mm^2	75.7 at H_v = 18 kg/mm^2
100	63.3 at H_v = 17 kg/mm^2	68 at H_v = 17 kg/mm^2
average	68	74

Dislocation climb controlled by lattice diffusion is an operative mechanism at the high temperature creep while dislocation climb controlled by core diffusion process is the rate controlling mechanism at low temperature creep. Mathew et al. [36] calculated the activation energy of lattice self-diffusion of pure Sn and it found to be 66 kJ/mol. Previous studies on the creep deformation on Sn–Bi solder alloys revealed that the activation energy fell in the range between 83 and 91 kJ/mol [37-39]. In the present study, the average activation energy values estimated in the two alloys A and B is comparable to the activation energy of 66 kJ/mol for the lattice self-diffusion of Sn [36,40].

IV. CONCLUSIONS

Influence of nanosized Sb_2O_3 particles addition on the microstructure and mechanical characteristics of Sn–3wt% Bi solder alloy was investigated in this study. Results showed that Sb_2O_3 nanoparticles addition enhances the hardness behavior of Sn–Bi solder. It was observed that the hardness values decreased gradually with the increase in aging temperature exhibiting maxima at 333 K. The stress exponent values ranging from 7 to 18 for both alloys. The mean activation energy values of both alloys A and B was found to be comparable to the activation energy for lattice self-diffusion of Sn.

REFERENCES

[1] Gain, A. K. and Y. C. Chan (2014), Growth mechanism of intermetallic compounds and damping properties of Sn-Ag-Cu-1wt% nano-ZrO_2 composite solders, Microelectron. Reliab., 54, 945-966.
[2] Abd El-Rehim, A. F. and H. Y. Zahran (2014), Effect of aging treatment on microstructure and creep behavior of Sn-Ag and Sn-Ag-Bi solder alloys, Mater. Sci. Technol., 30, 434-438.
[3] Osórioa, W. R., J. E. Spinelli, C. R. M. Afonsob, L. C. Peixotoc and A. Garciac (2011), Microstructure, corrosion behaviour and microhardness of a directionally solidified Sn-Cu solder alloy, Electrochim. Acta, 56, 8891-8899.
[4] Silva, B. L., A. Garcia, J. E. Spinelli (2016), Cooling thermal parameters and microstructure features of directionally solidified ternary Sn-Bi-(Cu,Ag) solder alloys, Mater. Character. 114, 30-42.
[5] Abd El-Rehim, A. F. (2008), Effect of grain size on the primary and secondary creep behavior of Sn-3 wt.% Bi alloy, J. Mater. Sci., 43, 1444-1450.
[6] Mitlin D., C. H. Raeder and R. W. Messler, Jr.(1999), Solid solution creep behavior of Sn-xBi alloys, Metall. Mater. Trans. A, 30, 115-122.
[7] Mahmudi, R., A. R. Geranmayeh, S. R. Mahmoodi and A. Khalatbari (2007), Room-temperature indentation creep of lead-free Sn-Bi solder alloys, J. Mater. Sci.: Mater. Electron., 18, 1071-1078.
[8] Lai, Z. and D. Ye (2016), Microstructure and fracture behavior of non eutectic Sn–Bi solder alloys, J. Mater. Sci.: Mater. Electron., 27, 3182-3192.
[9] Mahmudi, R., A. R. Geranmayeh, S. R. Mahmoodi and A. Khalatbari (2007), Effect of cooling rate on the room-temperature indentation creep of cast lead-free Sn-Bi solder alloys, phys. stat. sol. (a), 204, 2302-2308.
[10] Al-Ganainy, G. S., B. A. Khalifa, R. Afify and M. R. Nagy (1996), Effect of phase transformation on creep characteristics of Sn-5 wt% Bi alloy, phys. stat. sol. (a), 158, 463-469.
[11] Fawzy, A., S. A. Fayek, M. Sobhy, E. Nassr, M. M. Mousa and G. Saad (2014), Tensile creep characteristics of Sn-3.5Ag-0.5Cu (SAC355) solder reinforced with nano-metric ZnO particles, Mater. Sci. Eng.A, 603,1-10.
[12] Chang, S. Y., C. C. Jain,T. H. Chuang, L. P. Feng and L. C. Tsao (2011), Influence of TiO_2 nanoparticles on IMC growth in Sn-3.0Ag-0.5Cu-xTiO_2 solder joints during isothermal aging process, Mater. Des., 32, 4720-4727.
[13] Lee, H. T. and Y. H. Lee (2006), Adhesive strength and tensile fracture of Ni particle enhanced Sn-Ag composite solder, Mater. Sci. Eng. A, 419, 172-180.
[14] Shen, J., Y. C. Liu, Y. J. Han, Y. M. Tian and H. X. Gao (2006), Strengthening effects of ZrO_2 nanoparticles on the microstructure and microhardness of Sn-3.5Ag lead-free solder, J. Electron. Mater., 35, 1672-1679.
[15] Lee, C. W., Y. S. Shin and S. H. Yoo (2010), Effect of SiC nanoparticles dispersion on the microstructure and mechanical properties of electroplated Sn-Bi solder alloy, J. Nano Res., 11, 113-118.
[16] Yang, L., C. Du, J. Dai, N. Zhang and Y. Jing (2013), Effect of nanosized graphite on properties of Sn-Bi solder, J. Mater. Sci.: Mater. Electron., 24, 4180-4185.
[17] Abd El-Rehim, A. F. and H. Y. Zahran (2017), Investigation of microstructure and mechanical properties of Sn-xCu solder alloys, J. Alloys Compds, 695, 3666-3673.
[18] Lee, B-J., C-S. Oh and J-H. Shim (1996), Thermodynamic assessments of the Sn-In and Sn-Bi binary systems , J. Electron. Mater., 25, 983-991.
[19] Tai, F., F. Guo, Z. D. Xia, Y. P. Lei and Y. W. Shi (2010), Effects of nano-structured particles on microstructure and microhardness of Sn-Ag solder alloy, J. Mater. Sci.: Mater. Electron., 21, 702-707.
[20] Abd El-Salam, F., A. M. Abd El-Khalek, R. H. Nada and A. Fawzy (2008), Effect of silver addition on the creep parameters of Sn-7 wt% Bi alloy during transformation, Mater. Charac., 59, 9-17.
[21] Saad, G., F. Abd El-Salam and M. T. Mostafa (1984), Dependence of creep rate on grain diameter in Sn-0.5at.% Bi alloy, Surf. Technol., 22, 73-97.
[22] H. Mughrabi, Plastic Deformation and Fracture of Materials (New York: VCH), 1993, pp. 315.
[23] Ross, R. G. and L-C Wen (1994), Crack propagation in solder joints during thermal-mechanical cycling, J. Electron. Packag., 116, 68-75.
[24] Eid, E. A., A. N. Fouda and El-Shazly M. Duraia (2016), Effect of adding 0.5wt% ZnO nanoparticles, temperature and strain rate on tensile properties of Sn-5.0 wt% Sb-0.5 wt% Cu (SSC505) lead free solder alloy, Mater. Sci. Eng. A, 657, 104.
[25] Cullity, B. D. and S. R. Stock, "Elementary of X-ray Diffraction", Englewood Cliffs, 3rd ed., Prentice-Hall, New Jersey (2001) p.167-171.
[26] Abo Zeid, E. F. and A. Gaber (2012), Mechanical properties and precipitation behavior as a function of heat treatment of Al-4.4Cu-1.5Mg-0.6Mn-0.25Si (wt%) alloy, Int. J. Metall. & Mater. Sci. Eng., 2, 11-20.

[27] Jamaati, R., M. R. Toroghinejad, S. Amirkhanlou and H. Edris (2015), On the achievement of nanostructured interstitial free steel by four-layer accumulative roll bonding process at room temperature, Metall. Mater. Trans. A, 46, 4013-4019.
[28] Gashti, S.O., A. Fattah-alhosseini, Y. Mazaheri and M. K. Keshavarz (2016), Effects of grain size and dislocation density on strain hardening behavior of ultrafine grained AA1050 processed by accumulative roll bonding, J. Alloys Compds, 658, 854-861.
[29] Sargent, P. M. and M. F. Ashby (1992), Indentation creep, Mater. Sci. Tech., 8, 594-601.
[30] Nabarro, F. R. N. (2002), Creep at very low rates, Metall. Mater. Trans. A, 33, 213-2018.
[31] Bushroa, A. R., R. G. Rahbari, H. H. Masjuki and M. R. Muhamad (2012), Approximation of crystallite size and microstrain via XRD line broadening analysis in TiSiN thin films, Vacuum, 86, 1107-1112.
[32] Park, K. T., E. J. Lavernia and F. A. Mohamed (1990), High temperature creep of silicon carbide particulate reinforced aluminum, Acta Metall. Mater. 38, 2149-2159.
[33] Li, Y. and T. G. Langdon (1998), Creep behavior of a reinforced Al-7005 alloy: Implications for the creep processes in metal matrix composites, Acta Mater., 46, 1143-1155.
[34] Li, Y. and T. G. Langdon (1998), An examination of the effect of processing procedure on the creep of metal matrix composites, Mater. Sci. Eng. A, 245, 1-9.
[35] Khan, K. B., T. R. G. Kutty and M. K. Surappa (2006), Hot hardness and indentation creep study on Al-5% Mg alloy matrix–B4C particle reinforced composites, Mater. Sci. Eng. A, 427, 76-82.
[36] Mathew, M. D., H. Yang, S. Movva and K. L. Murty (2005), Creep deformation characteristics of tin and tin-based electronic solder alloys, Metall. Mater. Trans. A, 36, 99-105.
[37] H. L. Reynolds, Creep of two-phase microstructure for microelectronic applications, University of California, Berkeley CA, 1998, p. 98.
[38] Morris, J. W. Jr., J. L. F. Goldstein and Z. Mei (1993), Microstructure and mechanical properties of Sn-In and Sn-Bi solders, JOM, 45, 25-27.
[39] Reinikainen, T. and J. Kivilahti (1999), Deformation behavior of dilute SnBi (0.5 to 6 at. pct) solid solutions, Metall. Mater. Trans. A, 30,123-132.
[40] Mahmudi, R., A. R. Geranmayeh, M. Salehi and H. Pirayesh (2010), Impression creep of the rare-earth doped Sn–2%Bi lead-free solder alloy, J. Mater. Sci.: Mater. Electron. 21, 262-269.

AUTHORS

Shereen M. Abdelaziz obtained MSc and PhD in Physics (Materials Science) in 2003 and 2007 from Ain Shams University, Egypt. She has held research or/and academic positions at ASU (EGYPT), QU (KSA). Research interests are Phase transformation of metals and alloys, Mechanical properties of alloys, Microstructure, Cyclic stress conditions.

H. Y. Zahran obtained MSc and PhD in Physics (Materials Science) in 2006 and 2010 from Ain Shams University, Egypt. She worked at the Metallurgical Laboratory in the Department of Physics, Faculty of Education, Ain Shams University, as a demonstrator, assistant lecturer and a Lecturer. She had an academic position at King Khalid University, Saudi Arabia. Research interests include Mechanical properties of metals and alloys, Microstructure, Semiconductor materials, Nano-metal oxide thin films/powders, Organic materials, Bio-ceramics.

A. F. Abd El-Rehim obtained MSc and PhD in Physics (Materials Science) in 2000 and 2004 from Ain Shams University, Egypt. He attended the School of Materials, University of Manchester, UK, on June 2013 as a Visiting Postdoctoral Researcher. Whilst in attendance, He has been an integral member of the LATEST2 research project (Light Alloys towards Environmentally Sustainable Transport: 2nd Generation) and he has fully participated in all group work. He has held research or/and academic positions at UOM (UK), PSMCHS (KSA), Sanaa University (Yemen), ASU (EGYPT), KKU (KSA). Research interests are Phase transformation of metals and alloys, Mechanical properties of alloys, Nanostructures & Nanomaterials, Microstructure, Cyclic stress conditions.